High-pressure elastic properties of dolomite melt supporting carbonate-induced melting in deep upper mantle

Man Xu[a,b], Zhicheng Jing[b,1], Suraj K. Bajgain[c], Mainak Mookherjee[c], James A. Van Orman[a], Tony Yu[d], and Yanbin Wang[d]

[a]Department of Earth, Environmental, and Planetary Sciences, Case Western Reserve University, Cleveland, OH 44106; [b]Department of Earth and Space Sciences, Southern University of Science and Technology, 518055 Shenzhen, Guangdong, China; [c]Department of Earth, Ocean, and Atmospheric Sciences, Florida State University, Tallahassee, FL 32306; and [d]Center for Advanced Radiation Sources, The University of Chicago, Chicago, IL 60637

Edited by David Walker, Columbia University, Palisades, NY, and approved June 17, 2020 (received for review March 7, 2020)

Deeply subducted carbonates likely cause low-degree melting of the upper mantle and thus play an important role in the deep carbon cycle. However, direct seismic detection of carbonate-induced partial melts in the Earth's interior is hindered by our poor knowledge on the elastic properties of carbonate melts. Here we report the first experimentally determined sound velocity and density data on dolomite melt up to 5.9 GPa and 2046 K by in-situ ultrasonic and sink-float techniques, respectively, as well as first-principles molecular dynamics simulations of dolomite melt up to 16 GPa and 3000 K. Using our new elasticity data, the calculated V_P/V_S ratio of the deep upper mantle (~180–330 km) with a small amount of carbonate-rich melt provides a natural explanation for the elevated V_P/V_S ratio of the upper mantle from global seismic observations, supporting the pervasive presence of a low-degree carbonate-rich partial melt (~0.05%) that is consistent with the volatile-induced or redox-regulated initial melting in the upper mantle as argued by petrologic studies. This carbonate-rich partial melt region implies a global average carbon (C) concentration of 80–140 ppm. by weight in the deep upper mantle source region, consistent with the mantle carbon content determined from geochemical studies.

carbonate melt | sound velocity | equation of state | upper mantle | V_P/V_S ratio

Carbon, one of the most important chemical elements for life, energy, and climate, is widely distributed in the Earth's upper mantle, through the deep carbon cycle (1, 2). Due to the limited solubility of carbon in mantle minerals (3) and the relatively oxidized environment in the shallower part of the upper mantle (<~250 km) (4), carbon is mostly stored in forms of carbonate minerals as accessory phases in mantle rocks. Petrologic studies suggest that the presence of carbonates can dramatically lower the solidus of mantle rocks (5–8), thereby producing incipient carbonate-rich melts (carbonatite melts) in the deep upper mantle through either partial melting of carbonated lithologies (5, 6) or redox melting of upwelling reduced carbon domains (9). These carbonate-rich melts are efficient agents for mantle metasomatism due to their high mobility (10) and enrichment in various incompatible elements (11). The presence of carbonate melts in the upper mantle has been argued by a range of petrological and geochemical studies including the discovery of carbonate melt inclusions in gem-quality diamond (12), observations of CO_2-rich petit-spot volcanos (13), and the investigation of Mg isotope anomalies in mantle-derived melts (14), and has been suggested to be the cause for high electrical conductivity anomalies (15, 16) in the mantle. However, direct seismic detection of the existence and distribution of carbonate-rich partial melts has been hindered by our poor understanding of the elastic properties, such as sound velocity and density, of carbonate melts at high pressures.

Experimental measurements on the sound velocity and density of carbonate melts most relevant to Earth's upper mantle (1), including $CaCO_3$ (calcite), $MgCO_3$ (magnesite), and $CaMg(CO_3)_2$ (dolomite) melts, are essentially nonexistent due to experimental challenges. At room pressure, these melt properties cannot be determined directly because carbonates in the $CaCO_3$-$MgCO_3$ system undergo decarbonation reactions prior to melting. As a result, room-pressure sound velocity and density measurements are limited to $CaCO_3$-bearing alkali carbonate melts (17–19) (with a $CaCO_3$ mole fraction less than 0.5). At high pressures, only the density of $CaCO_3$ melt has been estimated, based on X-ray scattering measurements (20), but this method suffers from complex data analysis procedures for background correction and the assumptions involved. So far, most our knowledge on the compressibility and equation of state (EOS) of $CaCO_3$-$MgCO_3$ melts comes from several molecular dynamics (MD) simulations using either classical force fields (21–23), or first-principles density functional theory (DFT) (23–25). However, large discrepancies exist among these studies. For example, a discrepancy of up to 12% exists for the densities of $MgCO_3$ melt reported in the studies of refs. 23, 26, and the estimated pressure derivative of compressibility for $CaCO_3$ melt differs by more than 30% among the results of refs. 21–23, 26. These discrepancies in the simulation results highlight the need for direct high-pressure experiments to better understand the physical properties of these carbonate melts at deep Earth conditions.

Significance

Petrologic studies suggest that carbonate-rich melts are present in the Earth's upper mantle and play an important role in the deep carbon cycle. However, seismic detection of these melts is difficult due to the lack of understanding of the elastic properties of carbonate melts. Here we determined the sound velocity and density of dolomite melt at upper mantle conditions using high-pressure experiments and theoretical simulations. The calculated velocities of carbonate melt-bearing mantle using these new elasticity data were compared with global seismic observations. The result suggests that ~0.05% carbonate-rich melt can be pervasively present in the deep upper mantle, implying a global average mantle carbon concentration of 80-140 ppm.

Author contributions: M.X. and Z.J. designed research; M.X., Z.J., S.K.B., M.M., J.A.V.O., T.Y., and Y.W. performed research; M.X., Z.J., S.K.B., and M.M. analyzed data; and M.X. and Z.J. wrote the paper.

The authors declare no competing interest.

This article is a PNAS Direct Submission.

[1]To whom correspondence may be addressed. Email: jingzc@sustech.edu.cn.

This article contains supporting information online at https://www.pnas.org/lookup/suppl/doi:10.1073/pnas.2004347117/-/DCSupplemental.

First published July 20, 2020.

Here we report the first high-pressure experimental study on the density and sound velocity of a carbonate melt (dolomite composition, $CaMg(CO_3)_2$), as well as new FPMD simulation results on dolomite melt. Of all of the carbonate melt compositions, the dolomite composition is of primary interest for the upper mantle because it is close to the primary near-solidus carbonatite melt compositions at upper mantle conditions by melting of carbonated mantle lithologies (1, 5, 27). Using our sound velocity and EOS results for dolomite melt and those for diopside melt from reference (28), we calculated the compressional wave velocity (V_P) to shear wave velocity (V_S) ratio for melt-bearing mantle as a function of melt fraction and depth. Comparison of our calculated V_P/V_S ratio with that of the global seismic models (29–31) provides new insights into the possible distribution, composition, and amount of partial melts in the deep upper mantle.

To determine the sound wave velocity of dolomite melt, we conducted in situ ultrasonic measurements combined with synchrotron X-ray diffraction and imaging (32) at high pressures in a Kawai-type multianvil apparatus (*Methods*) (*SI Appendix*, Fig. S1). The melt sample was synthesized in situ by heating a sintered polycrystalline dolomite disk to temperatures above the melting temperature, with complete melting confirmed by observing changes in reflected ultrasonic signals (*SI Appendix*, *Text S1* and Fig. S2). We determined the length of the melt sample using X-ray radiographic imaging (Fig. 1*A*), and the round-trip travel time of compressional waves (no shear waves for liquids) through the sample by measuring the arrival time difference between the ultrasonic signals reflected from the top and bottom surfaces of the sample (32–34) (Fig. 1*B*). We conducted five different experimental runs to acquire the sound velocity data for dolomite melt (Fig. 2*A* and *SI Appendix*, Table S2). At 1837 K, the sound velocity for dolomite melt increases with pressure from 3757 m/s at 1.9 GPa to 4905 m/s at 5.9 GPa. At pressures below ~4 GPa, the sound velocity decreases slightly with temperature, and the effect of temperature on the sound velocity becomes negligible with further increases in pressure. The uncertainty in measured sound velocities is less than 1%, arising mostly from the uncertainties in the determination of the length of the molten sample from X-ray radiography.

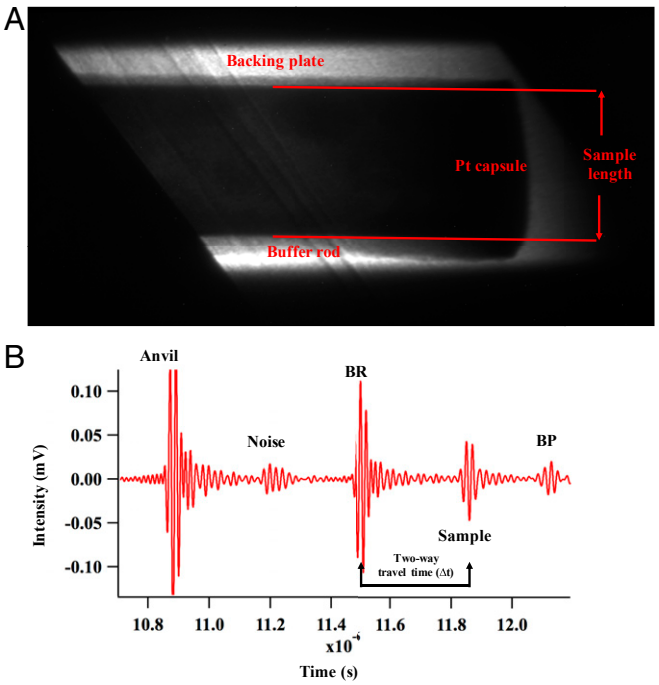

Fig. 1. (*A*) A representative radiographic image of the liquid sample at 4.1 GPa and 1733 K. Red lines indicate the positions of the buffer rod (BR)-sample and sample-backing plate (BP) boundaries. (*B*) Corresponding P-wave ultrasonic signals obtained for the dolomite melt sample.

We determined the density of dolomite melt at high pressures using the sink-float technique (38, 39) with boron carbide (B_4C) as the solid density marker in a Walker-type multianvil press (*Methods*). We have successfully observed neutrally buoyant and floating B_4C in dolomite melt at 3 and 5 GPa, respectively, whereas sinking of B_4C, expected at lower pressures, was not observed due to the decomposition of dolomite (40, 41) in the experiment performed at 1 GPa (*SI Appendix*, Fig. S3). The neutral buoyancy experiment allows us to estimate the density of dolomite melt to be 2.54 g/cm^3 at 3 GPa and 1773 K, using the EOS of B_4C (42). The uncertainty in the density is estimated to be ~1%, as bounded by the flotation case and the uncertainty in pressure is ~0.5 GPa.

We combined our sound velocity data with the density data point to constrain the EOS for dolomite melt (Fig. 2*B*) and obtained velocity as a function of pressure (Fig. 2*A*) based on the third-order isothermal Birch-Murnaghan EOS. We fit our experimental data using a Monte-Carlo approach (*SI Appendix*, *Text S2*), with best-fit results listed in Table 1. The calculated velocity and density profiles for dolomite melt recover the experimental data very well (Fig. 2). Our results provide strong constraints on the bulk modulus (K_{T0}) and its pressure derivative (K_T') (*SI Appendix*, Fig. S5), which are critical to extrapolating the sound velocity to deep upper mantle pressures. Compared to the velocity of diopside melt ($CaMgSi_2O_6$) (28), the velocity of dolomite melt is significantly faster than that of diopside melt at upper mantle conditions and the velocity difference between the two melts increases with pressure. This implies that carbonate melt may be less efficient than silicate melt in reducing the seismic velocity in the upper mantle of the Earth.

We supplemented our experimental data with first-principles molecular dynamics (FPMD) simulations on dolomite melt using the canonical (NVT) ensemble as implemented in the Vienna ab initio simulation package (VASP) (43–45) (*Methods*). We calculated the density and compressibility of dolomite melt at high pressures (*SI Appendix*, Table S3 and Fig. S6) employing both the local density approximation (LDA) and the generalized gradient approximation (GGA-PBE) (46, 47) for electronic exchange-correlation energy estimations. Both LDA and GGA produce density-pressure curves subparallel to the experimentally determined compression curve, with the experimental curve lying between the two (Fig. 2*B*). This is reasonable as it is well-known that LDA often overestimates the density while GGA underestimates it refs. 48, 49. Comparisons with other simulation results for dolomite melt (23, 26), density results for hydrous dolomite melt (35) and carbonated silicate melt (36, 37) are given in *SI Appendix*, *Text S4*. Similarly, both LDA and GGA simulations give similar pressure dependences of sound velocity. We find that the measured velocities of dolomite melt at high pressures are very well reproduced by our FPMD simulations using LDA (Fig. 2*A*), providing strong support for the extrapolation of the sound velocity to deep upper mantle pressures. Comparison of the results in the velocity-density space is shown in *SI Appendix*, Fig. S8.

Petrologic studies on melting of carbonated upper mantle have shown that the initiation of partial melting beneath mid-ocean ridges can occur as deep as ~220–330 km (5, 6). For typical mantle carbon concentrations of tens to hundreds of ppm, the determined carbonated mantle solidus is expected to be always lower than the upper mantle adiabat (50), implying a pervasive volatile-induced partial melting in the deep upper mantle. The small amount (<0.1%) of melt produced by melting of carbonated peridotite (1), or by redox melting of upwelling reduced carbon-enriched mantle (9) is likely to be carbonatite (with ~40 wt% CO_2) at a depth greater

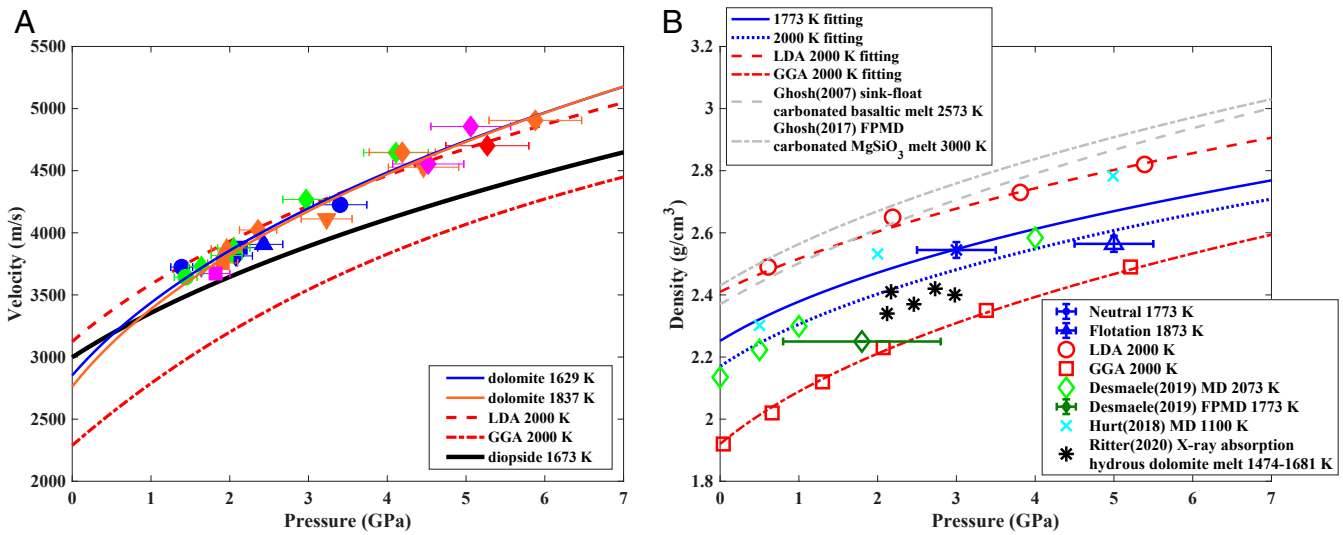

Fig. 2. (*A*) Sound velocity as a function of pressure for dolomite melt. Different markers correspond to different experimental runs: square-T2207, circle-T2208, upward-pointing triangle-T2261, downward-pointing triangle-T2262, diamond-T2439. Different marker colors correspond to different temperatures: blue-1629 K, green-1733 K, orange-1837 K, magenta-1942 K, red-2046 K. The blue and orange curves are fitted velocity results of dolomite melt along the 1629 K and 1837 K isotherms, respectively. The dashed and dash-dot curves are our FPMD results for dolomite melt along the 2000 K isotherm based on LDA and GGA, respectively. The thick black curve is the velocity profile for diopside melt from Xu et al. (28) for comparison. The diopside melt velocity is calculated along its adiabat with a potential temperature of 1673 K, but the temperature effect on the velocity of diopside melt at high pressures is negligible (28). (*B*) Density as a function of pressure for dolomite melt obtained from experiments and FPMD simulations in this study, and comparison with previous studies. Blue asterisk-neutral point, blue upward-pointing triangle-flotation point, blue solid line-EOS fitting based on experimental data at 1773 K, blue dotted line-EOS fitting at 2000 K, red circle-density data obtained by LDA, red square-density data obtained by GGA, red dashed line-EOS fitting at 2000 K for LDA, red dash-dot line-EOS fitting at 2000 K for GGA, green diamond-classical MD simulations data at 2073 K from Desmaele et al. (23), dark green diamond-GGA simulation data at 1773 K from Desmaele et al. (23), cyan cross-classical MD simulations data at 1100 K from Hurt (26), black star-density data of hydrous dolomite melt (with 10 wt% H_2O) at 1474–1681 K from Ritter et al. (35) measured by X-ray absorption method, gray dashed line-density of carbonated basaltic melt (with 5.0 wt% CO_2) from sink-float experimental results by Ghosh S. et al. (36), gray dash-dot line-density of carbonated $MgSiO_3$ melt (with 5.2 wt% CO_2) from FPMD results by Ghosh D.B. et al. (37).

than ∼300 km or carbonate-rich silicate melt (≤ 25 wt% CO_2 and ≥25 wt% SiO_2) at a shallower depth. Geodynamic modeling on the rates and distribution of carbonate melting using mantle upwelling patterns also shows that low-degree carbonate-induced melting occurs pervasively throughout the oceanic upper mantle at depths greater than ∼150 km (51). The presence of such carbonate-rich melt at greater depths (∼150–330 km) than typical silicate melting (less than ∼85 km deep) may well explain the observed deeper geophysical anomalies in the upper mantle (52–55), implying that carbonated incipient melting may extend to as deep as ∼300–330 km. However, no direct constraint from seismic velocity has ever been placed on the extent of this deep melting, due to the lack of available elasticity data on melts at high pressures. Here we employ the theoretical model for partially molten assemblages from Takei (56) and use our relaxed elasticity data on dolomite melt ($CaMg(CO_3)_2$) and previous results on diopside melt ($CaMgSi_2O_6$) (28) to evaluate the effect of partial melts on the seismic structure of the upper mantle.

We calculated V_P/V_S ratios for partially molten mantle (olivine + various amount of carbonate or silicate melt) as a function of depth (refer to *SI Appendix, Text S3* for calculation details), and compared the results with the V_P/V_S ratios from global 1-dimensional (1-D) seismic models including PREM (29), IASP91 (30), and AK135 (31) (Fig. 3). Three depth ranges in the upper mantle can be roughly distinguished based on the V_P/V_S ratio. From ∼50 to 80 km, the global seismic models display a higher V_P/V_S ratio than that of the dry mantle, which corresponds to the low-velocity zone (LVZ) near the lithosphere-asthenosphere boundary (LAB). Our modeling results are consistent with previous studies (57, 58) suggesting that a small amount of partial melts is required for the LVZ. In the depth range from ∼100 to 160 km, seismic models show V_P/V_S ratios close to or even smaller than

Table 1. P-T conditions and fitting results for the EOS of dolomite melt

	Experiments	GGA	LDA	Desmaele et al. (23)
$T_{ref}(K)$	1573	2000	2000	1653
$P(GPa)$	1.4–5.9	0–15	0–16	0–15
$T(K)$	1629–2046	2000–3000	2000–3000	1653–2073
$\rho_0(gcm^{-3})$	2.33 ± 0.02	1.92 ± 0.02	2.41 ± 0.01	2.26
$K_{T0}(GPa)$	16.1 ± 1.9	9.04 ± 1.56	19.87 ± 1.71	12.13
K'_{T0}	9.0 ± 1.5	6.45 ± 0.80	6.94 ± 0.45	8.5
δ_T	3.5 ± 1.3			
$(dP/dT)_V(MPa/K)$		$1.4 + 283.1e^{-6.8u}$	$7.5 - 5.8u$	
γ		$2.8 - 2.0u$	$3.3 - 2.6u$	

*$u = V/V_{ref}$ or ρ_{ref}/ρ.

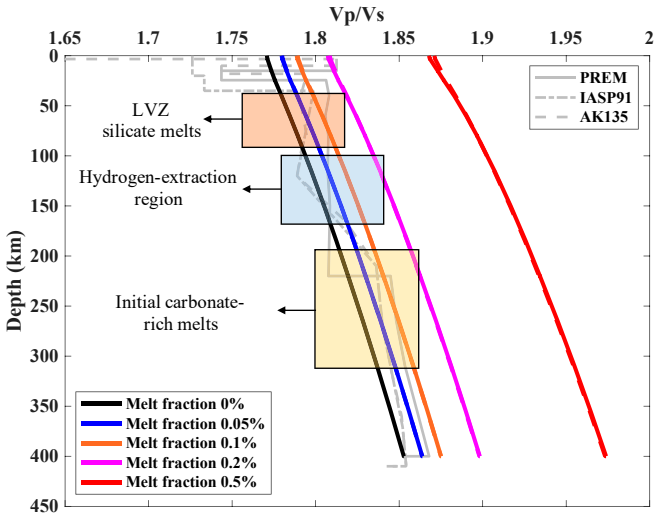

Fig. 3. V_P/V_S ratio calculated for a partially molten mantle analog as a function of depth and melt fraction, and its comparison with global seismic profiles. Colored solid lines-SC olivine + dolomite melt and colored dashed lines-SC olivine + diopside melt. They overlap at melt fractions less than 0.5%. The elastic properties for diopside melt is from Xu et al. (28). PREM model is from Dziewonski and Anderson (29), IASP91 model from Kennett and Engdahl (30) and AK135 model from Kennett et al. (31). All of the calculations were performed along a plausible mantle adiabatic temperature profile (61).

those of the melt-free mantle, probably due to the dehydration of this part of the mantle by low-degree partial melting above in the LVZ, as removal of hydrogen can also significantly affect the seismic velocity (59). In the deep upper mantle from ~180–330 km depth, the focus region in this study, all global seismic models show higher V_P/V_S ratios than that of the melt-free mantle and require the presence of a very small fraction (~0.05%) of either carbonate or silicate melt (Fig. 3). This implies that the initial melting in the upper mantle is indeed likely to extend as deep as ~330 km, consistent with previous petrologic studies on mantle melting (1, 5, 6). Although carbonate melt has significantly higher acoustic velocities than silicate melt at high pressures (Fig. 2*A*), our modeling results show that for such a small melt fraction, seismology is unlikely to be able to distinguish the melt composition (carbonate vs. silicate) based on the observed velocity anomalies. Thus, a combined evaluation from petrologic and mineral physics results are needed in order to better understand the nature and amount of the melts at these depths. According to the melt compositions determined from petrologic studies, the melt is most likely to be carbonatite melt (5) or carbonate-rich silicate melt (6). Our V_P/V_S modeling results thus support that a small fraction of carbonate-rich melt corresponding to the volatile-induced mantle incipient melting may be globally present in the deep upper mantle from ~180–330 km. Although the possible presence of silicate melt at these depths cannot be fully ruled out by our data, our preferred interpretation is the presence of carbonate-rich melt, since producing carbonate-free silicate melt at these depths requires much higher temperature than the mantle geotherm (60).

The pervasive presence of carbonate-rich melt is potentially at odds with some estimates of oxygen fugacity (fO_2) for the upper mantle below ~250 km (4, 9), where the average fO_2 is expected to decrease with depth and becomes too low for carbonates to be stable. However, a recent study (62) on mantle redox state using CO_2-trace element systematics of oceanic basalt shows that the convecting upper mantle is likely to be more oxidized than the fO_2 recorded in mantle xenoliths. In addition, the upper mantle at ~250–330 km depth could have significant heterogeneities with a variation of fO_2 at a given depth up to 2–4 orders of magnitude (63). This means that both reduced carbon (diamond or graphite) and oxidized carbonate can be stable at such depths. Furthermore, the melt present at these depths is likely to be a carbonate-silicate mixture rather than a pure carbonate melt. The lower CO_2 content of these melts increases their thermodynamic stability at depths below the pure carbonate redox front (64). Hence, a pervasive presence of carbonate-rich melt in the deep upper mantle is plausible, and this carbonate-rich melt region itself may be also a reflection of the redox-regulated incipient melting in the deep upper mantle. Stagno et al. (64) has developed a mantle redox state model based on oxythermobarometric equilibria of natural garnet peridotite rocks and demonstrated that the depth and thickness of redox melting is strongly dependent on the initial mantle $Fe^{3+}/\Sigma Fe$ ratio and carbon content. With gradual increase of Fe^{3+} in the mantle due to the subduction of oxidized materials, the redox melting front could be deepened (65). Our results based on global seismic model showing a large range of carbonate-induced melting depths may thus reflect the heterogeneities of upper mantle Fe^{3+} and carbon content.

Due to the low wetting angle (66) and high enrichment of incompatible elements in carbonate melt (11), the presence of even a very small amount of such melt will have a significant influence on the physical and chemical properties of the upper mantle. Even with fully connected melt networks, as is the case for carbonate melt (66), the very small fraction of melt is likely to be retained in the deep upper mantle for a long time due to a combination of low permeability and surface tension forces (67, 68), thus resulting in the high V_P/V_S ratio observed in the global seismic structures. Alternatively, carbonate-rich melt in deeper regions may migrate upwards, with gradual transition in composition to more silicate-rich melt (1), which could result in possible accumulations of melt at depth, due to an increase in melt viscosity (10). Recent viscosity measurements on carbonated silicate melts (69, 70) indeed show much higher viscosity and lower ascent rate than pure carbonate melts. These carbonated magmas may thus have a long residence time in the upper mantle, generating the observed seismic anomalies.

The pervasive presence of ~0.05% carbonate-rich melt provides a new way to estimate the global average carbon concentration in the deep upper mantle, a critical parameter for understanding the deep carbon reservoir. Although it is well-known that carbon distribution in the upper mantle is highly heterogeneous (71), a global average value for carbon content is still useful for planetary scale geochemical and geophysical modeling. Considering possible lateral heterogeneities in the mantle, it should, however, be noted that the integrated seismic signature over carbon heterogeneities such as V_P/V_S anomalies in the 1-D global models may not be produced by a simple mass-averaged carbon content when the mantle seismic velocity is a strongly nonlinear function of carbon content. However, a comprehensive analysis of lateral carbon content variation is difficult due to the lack of high-quality V_P/V_S seismic observations at these depths and is thus beyond the scope of current study. Assuming the melt is carbonatitic with an upper bound of ~40 wt% CO_2 (5), and employing the carbon partitioning coefficient between mantle melt and solid (0.00055 ± 0.00025) determined experimentally (72) and a batch melting model, the estimated average carbon (C) concentration in the deep upper mantle based on our constrained melt fraction is about 80–140 ppm by weight. This estimate lies between the carbon content estimated for a depleted mantle source (~10–30 ppm) and an enriched mantle source (~50–500 ppm) based on geochemical measurements of erupted basalts, associated melt inclusions and/or CO_2/incompatible elements systematics (1). This further supports the plausibility of a global presence of carbonate-rich partial melts in the deep upper mantle, probably corresponding to the effective base of volatile-induced/redox regulated incipient melting (71). This carbon concentration

amounts to an average carbon budget of ~(2.0–3.6) × 10^{19} kg in the deep upper mantle, roughly consisting of ~10% of the total mantle carbon budget (1), suggesting that the Earth's deep upper mantle is a significant reservoir for the deep carbon cycle.

Materials and Methods

Starting Materials. The samples used in both ultrasonic and sink-float experiments were synthetic dolomite cores provided by Dr. Caleb W. Holyoke III from the University of Akron. The dolomite was synthesized by the hot isostatic pressing method described in detail in previous studies (73, 74). The synthetic dolomite is fine-grained (2.5 ± 1.5 μm), has a uniform texture and a nearly perfect stoichiometric composition (73). For ultrasonic experiments, cylindrical disks with the desired diameter (1.7 mm) were machined from the synthetic dolomite chunk by using a CNC-milling machine. The top and bottom of the disks were then polished to mirror reflection (<1 μm) with nearly perfect parallelism. The polished disks were used as the starting materials for the ultrasonic experiments. For sink-float experiments, the dolomite chunk was crushed and ground to powders and stored in a vacuum oven before each experiment.

High-Pressure Ultrasonic Measurements. The high-pressure ultrasonic measurements were performed at the GSECARS Beamline 13-ID-D of the Advanced Photon Source, Argonne National Laboratory, using a 10-MN hydraulic press with a double-stage Kawai-type multianvil module (75). Tungsten carbide anvils with a truncation edge length of 8 mm were used as the second-stage anvils. An MgO-$MgAl_2O_4$ octahedron with an edge length of 14 mm was used as the pressure medium in each experiment. The detailed cell assembly is shown in *SI Appendix*, Fig. S1*A*. Pressure of the experiments was determined by energy-dispersive X-ray diffraction of the pressure marker consisting of a mixture of MgO and h-BN (MgO:BN = 3:1 by weight) in the cell assembly, using the EOS of MgO (76). The uncertainty in pressure is about 10%. Temperature of the experiments was estimated by a W5Re-W26Re thermocouple, with corrections for the thermal gradient calibrated on a similar cell assembly by Chantel et al. (77). The uncertainty in temperature is about 50 K.

The setup for ultrasonic measurements has been described in detail by Jing et al. (33) and Xu et al. (28). Elastic waves, converted from electrical signals in the frequency range of 20–60 MHz by a 10° Y-cut $LiNbO_3$ piezoelectric transducer attached to the corner of the bottom WC anvil, travel through the cell assembly, and are reflected at various interfaces including the anvil-buffer rod (BR), buffer rod-sample and sample-backing plate (BP) interfaces (see *SI Appendix*, Fig. S1*A* for positions of these interfaces). The reflected elastic waves are then converted back by the same transducer to electrical signals which are recorded by a digital oscilloscope at a sampling rate of 5 × 10^9/s. Travel time through the sample was determined by the pulse-echo overlap method (33, 34) using the reflected signals from BR-sample and sample-BP interfaces (Fig. 2*B*). The sound velocity is nearly independent of frequency from 20 to 60 MHz (*SI Appendix*, Table S2) and no S-wave signals were observed for the melt (*SI Appendix*, Fig. S2), indicating that the measured sound velocity for dolomite melt is fully relaxed (78) and can be directly compared with seismic wave velocity. Uncertainty in travel time is within ±0.2 ns, corresponding to a relative uncertainty of 0.2%. Sample length was determined by X-ray radiographic imaging (Fig. 2*A*), with an uncertainty within ±1.774 μm (1 pixel), corresponding to a relative uncertainty of 0.5%. Then, the sound velocity of the sample was calculated from travel time and sample length, with a total propagated uncertainty of less than ~1%. In this study, platinum was used as the sample capsule and densified Al_2O_3 rod as BR and BP, which have also been successfully used in room-pressure ultrasonic measurements on carbonate melts (19).

For each experiment, the ultrasonic measurements were carried out at one to four fixed hydraulic ram loads, corresponding to pressures from ~1.4–5.9 GPa and at temperatures from 1629 to 2046 K. After reaching the target load, the temperature was increased steadily to above the melting temperature of dolomite (41). With increasing temperature, the ultrasonic signals change as the state of the sample transforms from solid to partial melting and then to fully molten liquid (*SI Appendix*, Fig. S2). For each experiment, two to four heating cycles were performed and finally the sample was quenched by turning the heater power off.

Sink-Float Density Measurements. The sink-float technique has been widely used to determine the density of silicate melts at high pressures (38, 39). In this technique, the density of a melt is bracketed by the sinking and flotation of preloaded solid markers, with known density, in the melt. However, this technique has never been applied to carbonate melts due to the difficulty of finding a suitable solid marker for carbonate melts. In this study, we have tested a range of materials and found that boron carbide (B_4C), which is a superhard material and has a low room-pressure density (~2.52 g/cm^3) and high melting temperature (~3036 K), is an effective density marker for carbonate melts.

The experiments were performed in a Walker-type multianvil press at Case Western Reserve University using the COMPRES 14/8 cell assembly (79). The detailed cell assembly is shown in *SI Appendix*, Fig. S1*B*. A stepped heater was used to reduce the thermal gradient in the assembly and graphite, which has been widely used in various experiments for carbonate melts (10, 20), was used as the sample capsule. The powdered dolomite sample together with several B_4C spheres (Sigma-Aldrich, 98% purity, ~50–70 μm size) was packed and loaded into the graphite capsule. Then, the graphite capsule was inserted into the assembly and separated from the heater by an MgO sleeve. The high-pressure density of the solid markers was calculated using the experimentally determined EOS of B_4C (42). The pressure of the experiments was estimated based on the pressure-load relationship calibrated by the phase transitions of bismuth and SiO_2, and the uncertainty in pressure was estimated to be ~0.5 GPa. The temperature of the experiments was estimated based on the W5Re-W26Re thermocouple readings, believed to be accurate within ±20 K.

In each experiment, the sample was first compressed to the target load at room temperature and then heated to 1073 K at a rate of about 50 K/min. After that, the temperature was quickly raised to the target temperature (in less than 1 min) to minimize possible reactions between the sample and solid markers. The experiment was then kept at the target temperature, which is higher than dolomite melting temperature (41) for about 2 min to allow the settling of the solid markers. The ultra-low viscosity of dolomite melt, estimated to be in the range of 0.007–0.010 Pa s at about 3–5 GPa and 1633–1783 K (10), ensures fast settling of the solid markers within the experimental duration. After the experiment, the sample was quenched by turning off the heater power. The quenched sample was then mounted in epoxy and polished for inspection of density marker positions under an optical microscope.

SEM Analysis of Quenched Samples. The quenched samples from ultrasonic experiments were analyzed by a field-emission scanning electron microscope (SEM) at the Swagelok Center for Surface Analysis of Materials of Case Western Reserve University. The acceleration voltage and probe current were set at 10 kV and 3.7 nA, respectively. Back scattered electron (BSE) images of the samples show the typical quench texture for carbonate melt (*SI Appendix*, Fig. S4), indicating that the samples are fully molten. For experiments at pressures lower than ~2.5 GPa, a small amount of bubbles and MgO blobs were found from the BSE images and EDS elemental mapping (*SI Appendix*, Fig. S4). This is consistent with previous melting experiments on dolomite (40, 41) showing that dolomite melts incongruently at pressures below ~2.5 GPa, which produces a liquid phase plus a vapor phase and periclase (MgO). The MgO blobs sank to the bottom of the sample and partly reacted with the top of Al_2O_3 buffer rod to form spinel (*SI Appendix*, Fig. S4). Due to this incongruent melting at low pressures, the quenched melt composition is slightly more calcium-rich than the stoichiometric dolomite composition (*SI Appendix*, Table S1). The MgO blobs and bubbles are unlikely to significantly affect the velocity results, however, because they are present in low abundance.

First-Principles Molecular Dynamics Simulations. FPMD simulation on dolomite melt was performed in canonical (NVT) ensemble as implemented in the Vienna ab initio simulation package (VASP) (43–45). In FPMD simulations, the calculation of forces and energies are based on density functional theory (DFT) with the projector augmented-wave (PAW) method (80). For the estimation of electronic exchange-correlation energy, we used both the local density approximation (LDA) and the generalized gradient approximation (GGA-PBE) (46, 47). We used Γ-point sampling to integrate the Brillouin-zone with a time step of 1 fs. The Nosé thermostat algorithm provides a constant temperature in our MD simulations with a finite size of the plane wave basis set by energy cutoff of 450 eV (81). A volume dependent Pulay correction is added to the pressure to account for the use of limited cutoff energy, i.e., 450 eV (82).

$$P = P_{MD} + P_{Pulay}, \text{ where } P_{Pulay} = P_{Ecut=950eV} - P_{Ecut=450eV}$$

Pulay corrections for the explored range of pressure, 0–20 GPa, range from 0.6 to 1.0 GPa.

We used a crystalline dolomite with trigonal symmetry as an initial guess and then homogeneously strained the trigonal lattice to a cubic lattice and

melted dolomite at 4000 K. Straining of the lower symmetry unit cells of crystalline matter to a cubic lattice has been successfully used in previous FPMD studies (83, 84). We used a cubic unit cell with a reference volume (V_{ref} = 1157.62 Å^3) with eight formula units of $CaMg(CO_3)_2$. V_{ref} was chosen based on the ambient-pressure volume of carbonate melt (23). The density of $CaMg(CO_3)_2$ melt at the reference volume is 2.12 g/cm^3. After equilibrating the melt structure at 4000 K, the temperature was lowered to 3000 K. At 3000 K, simulations were performed along many constant volumes that correspond to pressures between 0 and 15 GPa. The dolomite melt was then cooled along an isochore to lower temperatures of 2600 K, 2500 K, 2300 K and 2000 K. Using a similar procedure, we also performed simulations using the GGA pseudopotential along 3000 K, 2500 K, and 2000 K isotherms. We used the Mie-Grüneisen thermal equation of state to describe the pressure, temperature and volume data obtained for dolomite melt from the simulations (*SI Appendix, Text S2*). All data supporting this study are presented in the paper and *SI Appendix*.

ACKNOWLEDGMENTS. This study was partly supported by the NSF (EAR-1619964 and 1620548) and the National Natural Science Foundation of China (41974098). The ultrasonic measurements were performed at GSECARS beamline 13-ID-D, Advanced Photon Source (APS), Argonne National Laboratory. GSECARS is supported by the NSF-Earth Sciences (EAR-1634415) and Department of Energy-GeoSciences (DE-FG02-94ER14466). This research used resources of the Advanced Photon Source, a U.S. Department of Energy (DOE) Office of Science User Facility operated for the DOE Office of Science by Argonne National Laboratory under Contract DE-AC02-06CH11357. S.K.B. and M.M. acknowledge funding from the NSF (EAR-1763215 and EAR-1753125) and XSEDE resources (TG-GEO170003). We thank Dr. Caleb W. Holyoke III for providing us the dolomite sample for the experiments. Nanthawan Avishai is thanked for her assistance on the SEM analysis of the quenched samples at the Swagelok Center for Surface Analysis of Materials (SCSAM) of CWRU. We thank the editor for handling our submission and two anonymous reviewers for constructive comments which help improve our manuscript substantially.

1. R. Dasgupta, M. M. Hirschmann, The deep carbon cycle and melting in Earth's interior. *Earth Planet. Sci. Lett.* **298**, 1–13 (2010).
2. T. Hammouda, S. Keshav, Melting in the mantle in the presence of carbon: Review of experiments and discussion on the origin of carbonatites. *Chem. Geol.* **418**, 171–188 (2015).
3. H. Keppler, M. Wiedenbeck, S. S. Shcheka, Carbon solubility in olivine and the mode of carbon storage in the Earth's mantle. *Nature* **424**, 414–416 (2003).
4. D. J. Frost, C. A. McCammon, The redox state of Earth's mantle. *Annu. Rev. Earth Planet. Sci.* **36**, 389–420 (2008).
5. R. Dasgupta, M. M. Hirschmann, Melting in the Earth's deep upper mantle caused by carbon dioxide. *Nature* **440**, 659–662 (2006).
6. R. Dasgupta *et al*., Carbon-dioxide-rich silicate melt in the Earth's upper mantle. *Nature* **493**, 211–215 (2013).
7. K. Litasov, E. Ohtani, The solidus of carbonated eclogite in the system CaO-Al_2O_3-MgO-SiO_2-Na_2O-CO_2 to 32 GPa and carbonatite liquid in the deep mantle. *Earth Planet. Sci. Lett.* **295**, 115–126 (2010).
8. S. Poli, Carbon mobilized at shallow depths in subduction zones by carbonatitic liquids. *Nat. Geosci.* **8**, 633–636 (2015).
9. A. Rohrbach, M. W. Schmidt, Redox freezing and melting in the Earth's deep mantle resulting from carbon-iron redox coupling. *Nature* **472**, 209–212 (2011).
10. Y. Kono *et al*., Ultralow viscosity of carbonate melts at high pressures. *Nat. Commun.* **5**, 5091 (2014).
11. J. Blundy, J. Dalton, Experimental comparison of trace element partitioning between clinopyroxene and melt in carbonate and silicate systems, and implications for mantle metasomatism. *Contrib. Mineral. Petrol.* **139**, 356–371 (2000).
12. A. M. Logvinova *et al*., Carbonatite melt in type Ia gem diamond. *Lithos* **342–343**, 463–467 (2019).
13. S. Machida, T. Kogiso, N. Hirano, Petit-spot as definitive evidence for partial melting in the asthenosphere caused by CO_2. *Nat. Commun.* **8**, 14302 (2017).
14. S. Li *et al*., Deep carbon cycles constrained by a large-scale mantle Mg isotope anomaly in eastern China. *Natl. Sci. Rev.* **4**, 111–120 (2017).
15. F. Gaillard, M. Malki, G. Iacono-Marziano, M. Pichavant, B. Scaillet, Carbonatite melts and electrical conductivity in the asthenosphere. *Science* **322**, 1363–1365 (2008).
16. D. Sifré *et al*., Electrical conductivity during incipient melting in the oceanic low-velocity zone. *Nature* **509**, 81–85 (2014).
17. Q. Liu, R. A. Lange, New density measurements on carbonate liquids and the partial molar volume of the $CaCO_3$ component. *Contrib. Mineral. Petrol.* **146**, 370–381 (2003).
18. S. M. Hurt, R. A. Lange, The density of Li_2CO_3-Na_2CO_3-K_2CO_3-Rb_2CO_3-Cs_2CO_3-$CaCO_3$-$SrCO_3$-$BaCO_3$ liquids: New measurements, ideal mixing, and systematic trends with composition. *Geochim. Cosmochim. Acta* **248**, 123–137 (2019).
19. M. C. O'Leary, R. A. Lange, Y. Ai, The compressibility of $CaCO_3$-Li_2CO_3-Na_2CO_3-K_2CO_3 liquids: Application to natrocarbonatite and CO_2-bearing nephelinite liquids from Oldoinyo Lengai. *Contrib. Mineral. Petrol.* **170**, 1–18 (2015).
20. J. Hudspeth, C. Sanloup, Y. Kono, Properties of molten $CaCO_3$ at high pressure. *Geochem. Perspect. Lett.* **7**, 17–21 (2018).
21. M. J. Genge, G. D. Price, A. P. Jones, Molecular dynamics simulations of $CaCO_3$ melts to mantle pressures and temperatures: Implications for carbonatite magmas. *Earth Planet. Sci. Lett.* **131**, 225–238 (1995).
22. S. M. Hurt, A. S. Wolf, Thermodynamic properties of $CaCO_3$-$SrCO_3$-$BaCO_3$ liquids: A molecular dynamics study using new empirical atomic potentials for alkaline earth carbonates. *Phys. Chem. Miner.* **46**, 165–180 (2018).
23. E. Desmaele, N. Sator, R. Vuilleumier, B. Guillot, The $MgCO_3$-$CaCO_3$-Li_2CO_3-Na_2CO_3-K_2CO_3 melts: Thermodynamics and transport properties by atomistic simulations. *J. Chem. Phys.* **150**, 214503 (2019).
24. R. Vuilleumier, A. Seitsonen, N. Sator, B. Guillot, Structure, equation of state and transport properties of molten calcium carbonate ($CaCO_3$) by atomistic simulations. *Geochim. Cosmochim. Acta* **141**, 547–566 (2014).
25. Z. Zhang, Z. Liu, High pressure equation of state for molten $CaCO_3$ from first principles simulations. *Chin. J. Geochem.* **34**, 13–20 (2015).
26. S. M. Hurt, *The Thermodynamic Properties and Structure of Alkali and Alkaline Earth Carbonate Melts*, (The University of Michigan, 2018).
27. M. E. Wallace, D. H. Green, An experimental determination of primary carbonatite magma composition. *Nature* **335**, 343–346 (1988).
28. M. Xu *et al*., Ultrasonic velocity of diopside liquid at high pressure and temperature: Constraints on velocity reduction in the upper mantle due to partial melts. *J. Geophys. Res. Solid Earth* **123**, 8676–8690 (2018).
29. A. M. Dziewonski, D. L. Anderson, Preliminary reference Earth model. *Phys. Earth Planet. Inter.* **25**, 297–356 (1981).
30. B. L. N. Kennett, E. R. Engdahl, Traveltimes for global earthquake location and phase identification. *Geophys. J. Int.* **105**, 429–465 (1991).
31. B. L. N. Kennett, E. R. Engdahl, R. Buland, Constraints on seismic velocities in the Earth from travel times. *Geophys. J. Int.* **122**, 108–124 (1995).
32. Z. Jing, T. Yu, M. Xu, J. Chantel, Y. Wang, High-pressure sound velocity measurements of liquids using in situ ultrasonic techniques in a multianvil apparatus. *Minerals (Basel)* **10**, 126 (2020).
33. Z. Jing *et al*., Sound velocity of Fe-S liquids at high pressure: Implications for the Moon's molten outer core. *Earth Planet. Sci. Lett.* **396**, 78–87 (2014).
34. Y. Kono *et al*., Simultaneous structure and elastic wave velocity measurement of SiO_2 glass at high pressures and high temperatures in a Paris-Edinburgh cell. *Rev. Sci. Instrum.* **83**, 33905 (2012).
35. X. Ritter *et al*., Density of hydrous carbonate melts under pressure, compressibility of volatiles and implications for carbonate melt mobility in the upper mantle. *Earth Planet. Sci. Lett.* **533**, 116043 (2020).
36. S. Ghosh, E. Ohtani, K. Litasov, A. Suzuki, T. Sakamaki, Stability of carbonated magmas at the base of the Earth's upper mantle. *Geophys. Res. Lett.* **34**, L22312 (2007).
37. D. B. Ghosh, S. K. Bajgain, M. Mookherjee, B. B. Karki, Carbon-bearing silicate melt at deep mantle conditions. *Sci. Rep.* **7**, 848 (2017).
38. C. B. Agee, Crystal-liquid density inversions in terrestrial and lunar magmas. *Phys. Earth Planet. Inter.* **107**, 63–74 (1998).
39. R. Knoche, R. W. Luth, Density measurements on melts at high pressure using the sink/float method: Limitations and possibilities. *Chem. Geol.* **128**, 229–243 (1996).
40. A. J. Irving, P. J. Wyllie, Subsolidus and melting relationships for calcite, magnesite and the join $CaCO_3$-$MgCO_3$ to 36 kb. *Geochim. Cosmochim. Acta* **39**, 35–53 (1975).
41. A. Buob, R. W. Luth, M. W. Schmidt, P. Ulmer, Experiments on $CaCO_3$-$MgCO_3$ solid solutions at high pressure and temperature. *Am. Mineral.* **91**, 435–440 (2006).
42. S. P. Dodd, G. A. Saunders, B. James, Temperature and pressure dependences of the elastic properties of ceramic boron carbide (B_4C). *J. Mater. Sci.* **37**, 2731–2736 (2002).
43. G. Kresse, J. Furthmüller, Efficiency of ab-initio total energy calculations for metals and semiconductors using a plane-wave basis set. *Comput. Mater. Sci.* **6**, 15–50 (1996).
44. G. Kresse, J. Furthmüller, Efficient iterative schemes for ab initio total-energy calculations using a plane-wave basis set. *Phys. Rev. B Condens. Matter* **54**, 11169–11186 (1996).
45. G. Kresse, J. Hafner, Ab initio molecular dynamics for liquid metals. *Phys. Rev. B Condens. Matter* **47**, 558–561 (1993).
46. D. M. Ceperley, B. J. Alder, Ground state of the electron gas by a stochastic method. *Phys. Rev. Lett.* **45**, 566–569 (1980).
47. J. P. Perdew, K. Burke, M. Ernzerhof, Generalized gradient approximation made simple. *Phys. Rev. Lett.* **77**, 3865–3868 (1996).
48. A. R. Oganov, S. Ono, Theoretical and experimental evidence for a post-perovskite phase of $MgSiO_3$ in Earth's D" layer. *Nature* **430**, 445–448 (2004).
49. Z. Wu, R. E. Cohen, D. J. Singh, Comparing the weighted density approximation with the LDA and GGA for ground-state properties of ferroelectric perovskites. *Phys. Rev. B Condens. Matter Mater. Phys.* **70**, 104112 (2004).
50. R. Dasgupta, Volatile-bearing partial melts beneath oceans and continents-where, how much, and of what compositions. *Am. J. Sci.* **318**, 141–165 (2018).
51. F. Clerc, M. D. Behn, E. M. Parmentier, G. Hirth, Predicting rates and distribution of carbonate melting in oceanic upper mantle: Implications for seismic structure and global carbon cycling. *Geophys. Res. Lett.* **45**, 6944–6953 (2018).
52. Y. J. Gu, A. L. Lerner-Lam, A. M. Dziewonski, G. Ekström, Deep structure and seismic anisotropy beneath the east pacific rise. *Earth Planet. Sci. Lett.* **232**, 259–272 (2005).
53. The MELT Seismic Team, Imaging the deep seismic structure beneath a mid-ocean ridge: The MELT experiment. *Science* **280**, 1215–1218 (1998).
54. D. Lizarralde, A. Chave, G. Hirth, A. Schultz, Northeastern Pacific mantle conductivity profile from long-period magnetotelluric sounding using Hawaii-to-California submarine cable data. *J. Geophys. Res.* **100**, 17837–17854 (1995).
55. B. Bagley, J. Revenaugh, Upper mantle seismic shear discontinuities of the Pacific. *J. Geophys. Res.* **113**, B12301 (2008).
56. Y. Takei, Effect of pore geometry on V_P/V_S: From equilibrium geometry to crack. *J. Geophys. Res.* **107**, 2043 (2002).
57. H. Kawakatsu *et al*., Seismic evidence for sharp lithosphere-asthenosphere boundaries of oceanic plates. *Science* **324**, 499–502 (2009).

58. J. Chantel *et al*., Experimental evidence supports mantle partial melting in the asthenosphere. *Sci. Adv.* **2**, e1600246 (2016).
59. D. R. Villagómez, D. R. Toomey, D. J. Geist, E. E. E. Hooft, S. C. Solomon, Mantle flow and multistage melting beneath the Galápagos hotspot revealed by seismic imaging. *Nat. Geosci.* **7**, 151–156 (2014).
60. M. M. Hirschmann, Mantle solidus: Experimental constraints and the effects of peridotite composition. *Geochemistry Geophys. Geosystems* **1**, 2000GC000070 (2000).
61. T. Katsura, A. Yoneda, D. Yamazaki, T. Yoshino, E. Ito, Adiabatic temperature profile in the mantle. *Phys. Earth Planet. Inter.* **183**, 212–218 (2010).
62. J. Eguchi, R. Dasgupta, Redox state of the convective mantle from CO_2-trace element systematics of oceanic basalts. *Geochem. Perspect. Lett.* **8**, 17–21 (2018).
63. G. M. Yaxley, A. J. Berry, A. Rosenthal, A. B. Woodland, D. Paterson, Redox preconditioning deep cratonic lithosphere for kimberlite genesis - evidence from the central Slave Craton. *Sci. Rep.* **7**, 30 (2017).
64. V. Stagno, D. O. Ojwang, C. A. McCammon, D. J. Frost, The oxidation state of the mantle and the extraction of carbon from Earth's interior. *Nature* **493**, 84–88 (2013).
65. V. Stagno, Carbon, carbides, carbonates and carbonatitic melts in the Earth's interior. *J. Geol. Soc. London* **176**, 375–387 (2019).
66. W. G. Minarik, E. B. Watson, Interconnectivity of carbonate melt at low melt fraction. *Earth Planet. Sci. Lett.* **133**, 423–437 (1995).
67. B. K. Holtzman, Questions on the existence, persistence, and mechanical effects of a very small melt fraction in the asthenosphere. *Geochem. Geophys. Geosyst.* **17**, 470–484 (2016).
68. K. Selway, J. P. O'Donnell, A small, unextractable melt fraction as the cause for the low velocity zone. *Earth Planet. Sci. Lett.* **517**, 117–124 (2019).
69. V. Stagno *et al*., The viscosity and atomic structure of volatile-bearing melilititic melts at high pressure and temperature and the transport of deep carbon. *Minerals (Basel)* **10**, 267 (2020).
70. V. Stagno *et al*., "The viscosity of carbonate-silicate transitional melts at earth's upper mantle pressures and temperatures, determined by the in situ falling-sphere technique" in *Carbon in Earth's Interior, Geophysical Monograph 249*, G. E. Manning, J.-F. Lin, W. L. Mao, Eds. (John Wiley & Sons, Inc., First Edition, 2020), pp. 223–236.
71. M. Le Voyer, K. A. Kelley, E. Cottrell, E. H. Hauri, Heterogeneity in mantle carbon content from CO_2-undersaturated basalts. *Nat. Commun.* **8**, 14062 (2017).
72. A. Rosenthal, E. H. Hauri, M. M. Hirschmann, Experimental determination of C, F, and H partitioning between mantle minerals and carbonated basalt, CO_2/Ba and CO_2/Nb systematics of partial melting, and the CO_2 contents of basaltic source regions. *Earth Planet. Sci. Lett.* **412**, 77–87 (2015).
73. N. E. Davis, A. K. Kronenberg, J. Newman, Plasticity and diffusion creep of dolomite. *Tectonophysics* **456**, 127–146 (2008).
74. C. W. Holyoke, A. K. Kronenberg, J. Newman, Dislocation creep of polycrystalline dolomite. *Tectonophysics* **590**, 72–82 (2013).
75. Y. Wang *et al*., The large-volume high-pressure facility at GSECARS: A "Swiss-army-knife" approach to synchrotron-based experimental studies. *Phys. Earth Planet. Inter.* **174**, 270–281 (2009).
76. Y. Tange, Y. Nishihara, T. Tsuchiya, Unified analyses for *P* - *V* - *T* equation of state of MgO: A solution for pressure-scale problems in high *P* - *T* experiments. *J. Geophys. Res.* **114**, B03208 (2009).
77. J. Chantel, Z. Jing, M. Xu, T. Yu, Y. Wang, Pressure dependence of the Liquidus and solidus temperatures in the Fe-P binary system determined by in situ ultrasonics: Implications to the solidification of Fe-P liquids in planetary cores. *J. Geophys. Res.* **123**, 1113–1124 (2018).
78. M. L. Rivers, I. S. E. Carmichael, Ultrasonic studies of silicate melts. *J. Geophys. Res.* **92**, 9247–9270 (1987).
79. K. D. Leinenweber *et al*., Cell assemblies for reproducible multi-anvil experiments (the COMPRES assemblies). *Am. Mineral.* **97**, 353–368 (2012).
80. G. Kresse, D. Joubert, From ultrasoft pseudopotentials to the projector augmented-wave method. *Phys. Rev. B Condens. Matter Mater. Phys.* **59**, 1758–1775 (1999).
81. S. Nosé, A unified formulation of the constant temperature molecular dynamics methods. *J. Chem. Phys.* **81**, 511–519 (1984).
82. G. P. Francis, M. C. Payne, Finite basis set corrections to total energy pseudopotential calculations. *J. Phys. Condens. Matter* **2**, 4395–4404 (1990).
83. S. K. Bajgain, Y. Peng, M. Mookherjee, Z. Jing, M. Solomon, Properties of hydrous aluminosilicate melts at high pressures. *ACS Earth Space Chem.* **3**, 390–402 (2019).
84. L. Stixrude, B. Karki, Structure and freezing of $MgSiO_3$ liquid in Earth's lower mantle. *Science* **310**, 297–299 (2005).